SAND2014-2708C

ILASS Americas 26th Annual Conference on Liquid Atomization and Spray Systems, Portland, OR, May 2014

Measuring transient entrainment rates of a confined vaporizing diesel jet

W. E. Eagle*, M. P. B. Musculus
Sandia National Laboratories
Livermore, CA 94550, USA

L-M. C. Malbec, and G. Bruneaux
IFP Énergies nouvelles (IFPEN)
Rueil-Malmaison, France

Abstract

Partially premixed combustion strategies for compression-ignition engines reduce soot formation in part by extending the ignition delay to provide more time for mixing before combustion. However, vapor-fuel concentration measurements have shown that near-injector mixtures become too lean to achieve complete combustion, leading to an increase in unburned hydrocarbon emissions compared to conventional diesel combustion. One potential cause of the over-leaning is an "entrainment wave," which is a transient increase in local entrainment after the end of injection that has been predicted by a one-dimensional (1D) free-jet model. No previous measurements at diesel injection conditions have demonstrated conclusively that this entrainment wave exists, nor has its magnitude been verified. Using particle image velocimetry (PIV) in the ambient gases, we measure entrained gas flows through a diesel jet boundary before and after the end of injection. The entrainment calculation depends on the definition of the jet boundary, and we propose a definition for this boundary based on the local minimum in the product of the radial coordinate and the radial velocity (rv_r). We demonstrate that the method is robust for calculating entrainment in the presence of axial flow gradients in the ambient gases outside the jet. Prior to the end of injection, the measured portions of the quasi-steady jet exhibit steady entrainment rates that agree well with typical non-reacting gas-jet behavior, as well as with the 1D free-jet model. After end of injection, the local entrainment rate temporarily increases by as much as a factor of two, which is similar to the factor of 2.5 peak increase predicted by the 1D model. However, the entrainment wave is more broadly distributed in the experimental data, likely due to jet confinement or other real-jet processes absent in the 1D model.

---

*Corresponding author: weeagle@sandia.gov

Introduction

Turbulent jets of fluid are useful for many practical applications where mass and/or momentum need to be transferred rapidly from one fluid to another. We can estimate the local momentum transfer by directly measuring an increase in mass flow in the vicinity of a jet. For the case of incompressible, non-reacting jets, an increase measured mass flow in the jet must arise from induction, or 'entrainment,' of the surrounding fluid into the jet. Since entrainment must occur dynamically, we are interested in what variables control the transient local 'entrainment rate.' A brute-force numerical solution to the fully coupled Navier-stokes equations could provide a prediction of the locally-driven time-dependent process of entrainment, but at significant computational cost. On the other hand, however, the widespread use of turbulent jets and the similarity of different jets across a wide range of flow scales demonstrates both a need and plausibility of a simplified treatment. From a fundamental perspective, we would like to predict entrainment along the jet boundary, directly at the interface between the jet and the ambient fluid, and so predict the mixing state throughout the jet (Nickels & Perry, 1996). However, we are impeded by two major issues. One is a diversity of possible definitions for the jet boundary, particularly in the case of a transient injection. The second is a lack of relevant entrainment measurements for developing jets, or in the case of a steady jet, accurate measurements of local entrainment in the near field.

On dimensional grounds, for an axisymmetric jet, the local entrainment mass flow $\dot{m}_E(z)$ $[kg/m \cdot s]$ depends on only four global variables, the velocity, jet diameter, density and viscosity $(v(t), d, \rho, \mu)$. Individual variation in these parameters can be assessed through the jet Reynolds number, $Re = \rho v d/\mu$. For large values of Re, a free-jet develops 'self-similar' behavior some distance downstream of an initial 'transition' region, and the mixing rate also becomes independent of viscosity (Curtet and Ricou, 1964). In this region, the entrainment rate, and therefore the jet expansion angle hence mixing, or vice-versa) under 'self-similar' development can be found in textbooks on the subject of turbulent jets (for example, Abramovich, 1963) that survey hundreds monographs on the theory of submerged (no-coflow), co-flow, and counter-flowing jets. Each contribution furthers our understanding by attempting to predict or explain mixing via the entrainment of mass during the diffusion of momentum in various special engineering and environmental flows of interest.

The example of interest in this paper is the mixing of fuel and air in direct-injection diesel engines. Knowledge of the injection rate schedule and the local entrainment is critical to properly design an injection strategy that achieves a desired mixing state. Insufficient mixing leads to locally rich regions that contribute to smoke (carbonaceous soot) and other smog (nitrogen oxides) emissions. Non-conventional diesel combustion strategies like partially premixed combustion aim to increase mixing before combustion to reduce overall in-cylinder stoichiometry, yielding lower emissions of soot and nitrogen oxides; however, improvements in performance and/or reduction in emissions remain limited by the mixing rate (O'Connor & Musculus, 2013).

Another complication in determining the mixing rate is the transient end of injection. Deceleration of flow at the jet orifice has been shown to significantly change jet mixing and entrainment (Boree, Atassi, & Charnay, 1996). Following an orifice flow reduction, experiments indicate a transient increase in entrainment at the jet boundary relative to a steady jet. An increase in local mixing can yield locally fuel-lean mixtures, for which combustion may not proceed to completion, leading to increases in the emission of unburned hydrocarbons and carbon monoxide (Musculus, Miles, & Pickett, 2013).

For our engineering application of interest, lessons learned for gaseous jets can be extended to liquid-fuel sprays by accounting for differing densities of ambient and injected fluids. Successful predictions for transient spray penetration and mixing behavior are possible under the condition that entrainment is well predicted (Desantes, Arrègle, López, & Cronhjort, 2006; Iyer & Abraham, 2005; Siebers, 1999). As a result of applying a fixed spreading angle, these models enforce a *local* entrainment rate (to be defined later) to close the mass and momentum balance at the jet boundary. Hence, agreement of model predictions with experiments that measure penetration or entrainment requires the spray spreading angle be known a priori, or tuned empirically. Furthermore, these simple models assume a quiescent and unbounded ambient. This assumption is violated in the case of confined engine combustion chambers.

An important advancement in our understanding of jet entrainment and mixing is the predominant role of instantaneous large-scale structures on local mixing and entrainment (Dahm & Dimotakis, 1987; Philip & Marusic, 2012). Unlike an increase in laminar-like diffusion implied by a 'turbulent diffusivity' in the Reynolds analogy, large-scale structure in the flow implies that the local entrainment rate must instead be understood as a convolution of the contact surface and diffusive mixing. Therefore, two processes that control entrainment rate are the large-scale local-stretching between fluids (contact surface production) and the rapid mixing occurring at the smallest scales of the flow (contact surface consumption). To understand the entrainment process, we have to understand the dynamics of the jet boundary.

Progress may be made on dimensional grounds, if we simply assume that the stretching of the local jet surface obeys the same time-average axisymmetry as the jet. Invoking the assumption that axial momentum is only lost due to ambient fluid entrainment (no significant axial pressure gradients), growth of the local entrainment surface is the sole source of momentum transfer. The local surface area can be estimated as $2\pi r_b$, where r_b is the radius from the jet axis to the 'jet boundary,' through which the entrainment is occurring. We know, for example, in the case of turbulent self-similar flow, the stretching rate of the boundary (jet spreading angle) becomes constant (entrainment rate as well), implying equilibrium exists with production slightly outpacing consumption at large Reynolds numbers. Meanwhile, laminar jet fountains produce streams of liquid with nearly constant radius. Intuition suggests that therefore that local entrainment rate can be functionalized on the basis of the gradient in the local jet boundary radius, $\partial r_b/\partial z$. That is, for any given entrainment, the radius r_b should necessarily increase with downstream distance. Likewise, in the case of zero entrainment, r_b should remain constant. Therefore, a method is desired to accurately determine the jet boundary as an indication of, and a consequence of, entrainment. Unfortunately, as previously mentioned, theoretical determination of the form for the jet boundary in the near field remains an open question.

To address definitions of the jet boundary, we revisit the literature on entrainment and examine how defining the jet boundary affects the quantification of entrainment (Bisset, Hunt, & Rogers, 2002; Han & Mungal, 2001; Moon, Matsumoto, & Nishida, 2009; Ricou & Spalding, 1960). We focus on the case of an axisymmetric jet in cylindrical coordinates (r,θ,z) and examine the consequences of integrating over differential volume flux field (rv_r) $[(m^3/s)/m]$ to see how different definitions of the jet boundary affect the quantification of local jet entrainment. Heat release and compressibility are potential sources/sinks of volume flux in the general case, as is momentum loss due to pressure gradients, including drag forces; however quantifying these effects remains outside the scope of the current work.

For the engineering flow of interest, particle-image velocimetry (PIV) and laser-Doppler velocimetry (LDV) data have provided insight into entrainment in diesel-like jets including non-vaporizing (Rhim & Farrell, 2000), vaporizing (Kozma & Farrell, 1997; Milano, Brunello, & Coghe, 1991) and confined sprays (Post, Iyer, & Abraham, 2000; Singh, Sundararajan, & Bhaskaran, 2003). Recently, PIV data using 2µs pulse separation in a transient vaporizing diesel jet were analyzed to quantify entrainment using the axial gradient in the interior of the jet to compute the mass flux (Malbec & Bruneaux, 2010). Here, we extend this PIV image dataset to the relatively slow ambient gases outside the jet by using the larger pulse separation (100µs) that is available from the same experiment. We aim to directly quantify entrainment through the jet boundary using velocity measurements in the ambient gases thereby avoiding the large (correlated) fluctuations in velocity and density that exist inside the jet.

Our second aim is to provide the first experimental evidence for a transient increase in entrainment after the end of injection that has been predicted by simple one-dimensional (1D) jet models (Musculus & Kattke, 2009, Musculus 2009). Higher-fidelity large-eddy simulation (LES) of a transient air jet has provided confirmation of this as well, and additionally provides some clues to the dynamic process (larger vortex pairing motion) that leads to this end-of-injection entrainment increase (Hu, Musculus, & Oefelein, 2010). However, no other experimental measurements of entrainment increase after the end of injection are yet available. Therefore, we compare the entrainment measurements during and after end of injection to predictions of 1D transient jet entrainment model for diesel jets (Musculus & Kattke, 2009).

Experimental methods

The vaporizing spray experiments are performed at IFP Énergies nouvelles (IFPEN) in a constant-volume vessel simulating the conditions near top-dead-center in a compression-ignition engine (Malbec *et. al.,* 2013). The interior of the optical chamber is a cube, 12cm^3, with windows in the cube faces for laser and imaging access (**Fig. 1**). Within the vessel, high ambient temperatures are achieved through the combustion of a flammable gas mixture. The injection is triggered when the desired chamber temperature is reached during the cool-down of the combustion products. Initial pressure and composition (before the combustion event) are selected to obtain the desired temperature, density, and oxygen concentration at the moment of injection. For this experiment, non-combusting but vaporizing conditions are desired, for which the temperature, density, and oxygen concentration are 900K, 22.8kg/m^3, and 0%.

The horizontally mounted fuel injector on this vessel is the single-hole Bosch injector (#210678) from the Engine Combustion Network (ECN). Fuel pressure is controlled with a pneumatic pump, and the fuel is provided through a common rail, following ECN recommendations (Malbec & Bruneaux, 2010). The fuel is n-dodecane, which has a density of 703kg/m^3 at the experimental conditions. The fuel pressure is set at 1500bar, and the energizing duration of the injector is 2.795ms (actual injection duration is 4.3ms). The steady-state average mass flux through the injector is 2.25g/s, and the nozzle has a 0.0886mm orifice diameter. Uncertainties for these operating conditions and set points are available online, via the ECN ("Engine Combustion Network").

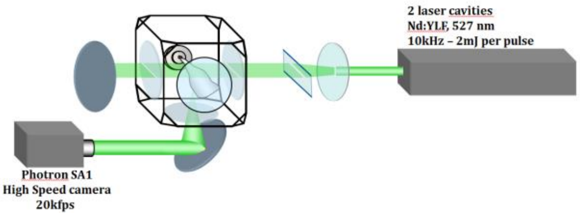

Figure 1. Experimental schematic, showing high-speed pulsed laser (right) directing a beam through sheet forming optics to the optical combustion chamber fitted with a diesel fuel injector (middle), and high-speed camera for PIV image acquisition (bottom-left).

Illumination is provided by a double-pulsed two-cavity 527nm YLF laser. Each laser cavity is operated at 10kHz. The optical setup is shown in **Fig. 1**. A 1mm thick, 64mm wide horizontal laser sheet is formed by the combination of spherical and cylindrical lenses, and intercepts the spray axis horizontally, in the focal plane of the camera. The time delay between consecutive pulses from the two laser cavities is 2µs, whereas 100µs elapses between 2 pulses from the *same* laser cavity. Resolving the low-velocity region in the ambient gases using the long pulse separation allows us to better estimate entrainment at the jet boundary than with short pulse separation.

A Photron SA1 high-speed camera equipped with a Nikkor 50mm f/1.2 lens and an 8mm extension ring collects the Mie-scattered laser light off the particles. (A discussion of particle Stokes-number appears in the Limitations and uncertainty section.) The camera acquires images at 20kHz with an exposure time of 50µs. Since subsequent pulses from the same cavity are used here, the effective acquisition rate of the new dataset is 10kHz. The size of the images is 448x592 pixels, with a resolution of 8 pixels per mm [56 x 74mm]. For the image in **Fig. 2**, the injector tip is 7mm outside the field of view, and the jet propagates downward along the centerline in this perspective. The top 13mm of the field of view is not illuminated by the laser sheet; therefore, the reported PIV data exist between 20mm and 80mm downstream of nozzle orifice.

The commanded start of injection is used a reference time and first image exposure is triggered off this signal. The injector experiences a physical delay of approximately 350µs before starting to inject fuel, such that the first image of the liquid spray in the field of view occurs at 400µs. An example image is shown in **Fig. 2**, 1700µs after the commanded start of injection.

We use the LaVision suite (DaVis 8) for processing the raw images. A multi-pass windowing procedure computes correlations at 64x64 pixels followed by 16x16 pixels and good vectors are selected using median filtering. Outside the spray, the procedure yields in excess of 95% good vectors. To obtain statistically meaningful ensemble velocity fields, 40 injections are averaged in the data presented here.

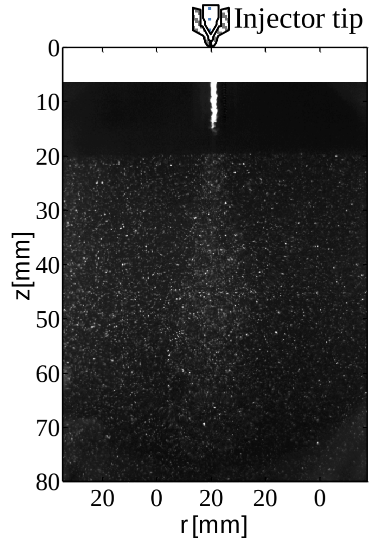

Figure 2. Representative raw PIV image, acquired 1700µs after the commanded start of injection. The injector is 7mm above top-center of the image, and the spray propagates downward in the perspective of this image. The top 13mm of the field of view is not directly illuminated by the laser sheet, but scattering of stray light off the liquid fuel spray is visible near the top.

Entrainment quantification

The desire to quantify entrainment has inspired previous authors to propose integral formulations based on control-volume analyses of mass and momentum fluxes (Han & Mungal, 2001; Musculus & Kattke, 2009; Ricou & Spalding, 1960). The common approach of these analyses is that the increase in axial mass flux within the jet with increasing downstream distance is attributed to entrainment of ambient gases outside the jet entering at the roughly conical jet-boundary. Assuming non-reacting, incompressible flow, the entrainment rate may be determined either by inferring it from measurements of the change in the axial mass flux within the jet, or by direct measurement of the induced ambient flow through the boundary between the jet and the ambient.

For the case of a liquid-fuel jet injected into the compressed gases of a reciprocating engine, the axial-mass-flux method is hampered by uncertainties including significant correlated turbulent density and velocity fluctuations, amplified by the fact that injected and ambient fluids have much different densities (700-

850 vs 15-50 kg/m^3). Direct entrainment measurements in the ambient fluid avoid this complication, because the density and velocity fluctuations are comparatively much smaller.

For the ambient entrainment measurements, however, the principle concern and source of uncertainty is the choice of a suitable control volume. A series of frustum (truncated cone) control volumes are shown in **Fig. 3**. By analyzing the flow through the boundaries of each of the control volumes, the variation in entrainment along the jet axis can be quantified. Determining an appropriate position for the upper and lower boundaries for each control volume is straightforward, but an a priori determination of the jet boundary on the side of each control volume remains an unresolved theoretical challenge.

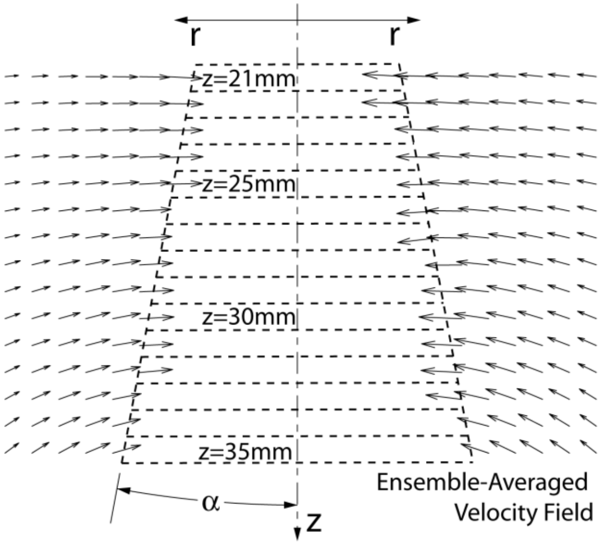

Figure 3. A series of frustrum-shaped control volumes surrounding the jet flowing from top to bottom. Example ensemble-averaged ambient flow vectors are included, acquired 1700μs after the commanded start of injection.

Typically, previous analyses have assumed that the ambient fluid flow outside the jet boundary is axially invariant (e.g. uniform co-flow or axially stagnant). In that case, a control surface of any shape that encompasses the same portion of the jet (dz) admits the same radial entrainment mass. That is, differences in the measured entrained flow at the boundary come exclusively from axial variation in radial entrainment, and therefore the entrainment mass flux unchanged as the control surface's radius from the jet axis is increased (Han & Mungal, 2001; Ricou & Spalding, 1960). However, for a large fraction of practical jet applications, the assumption of axial invariance cannot hold.

In the present experiment, the jet is confined by the chamber, and chamber-scale recirculation flows induced by the jet unavoidably generate axial flow variations in the ambient, even if the chamber is initially quiescent before a transient jet is initiated. Even for unconfined jets, the ambient flows may not be axially invariant, and back-flowing streamlines are visible near the jet boundary, especially as the jet is developing (Van Dyke, 1982). In either case, *when axial variations are present in the ambient, the distribution of entrainment computed at each axial location necessarily depends on the radial position of the control surface at the jet boundary*.

It is reasonable to expect that locating the control volume surface as close as possible to the true jet boundary (r_b) should provide the most physically meaningful quantification of local entrainment. Alternatively, entrainment could be measured significantly outside the jet boundary if it could be accurately mapped to the correct location on the jet boundary. Han and Mungal proposed one method for doing so by defining a frustum-shaped control volume with a judiciously selected cone angle (Han & Mungal, 2001). Appealing to continuity arguments for axial invariance, they argued that the appropriate frustum cone angle is that which yields a constant entrainment flow as the radius of the frustum was increased. In this way, they could measure entrainment well outside the turbulent jet boundary where they could be certain that velocity and density fluctuations were insignificant. However, this approach ignored the possibility of axial gradients existing outside the jet.

The derivations of both Ricou and Spalding (1960) and Han and Mungal (2001) define entrainment as the axial change in axial mass flux in the jet. From equation 11 of Han and Mungal (2001), the change in jet axial mass-flux $\dot{m}_E$ from one axial location z_1 to another location z_2 farther downstream (i.e., through the top and bottom surfaces of the control volumes in **Fig. 3**) can be expressed as

$$\dot{m}_E = \int_0^\infty 2\pi\overline{\rho v_z(z_2,r)}rdr - \int_0^\infty 2\pi\overline{\rho v_z(z_1,r)}rdr \qquad (1),$$

where $\overline{\rho v_z(z,r)}$ is the time-mean product of density ρ and axial velocity v_z, and r is the radial coordinate. Recall that in our definition, jet entrainment occurs through the jet boundary surface (**Fig. 3**), and therefore although integral in **Eqn. 1** extends to infinity, it is only necessary to compute to the jet boundary, r_b (The value of entrainment varies in the integration only so long as gradients of axial velocity persist). If *the ambient is assumed to have zero axial velocity gradient*, **Eqn. 1** effectively defines the jet boundary as the radial position where the axial velocity first obtains a positive axial gradient ($\partial v_z/\partial z > 0$). However, the calculation of gradient quantities, particularly in turbulent, unsteady flows is challenging. Therefore, we seek a theoretical link between this velocity gradient (second-order) and the primitive variables measured directly by PIV.

From continuity in an axisymmetric incompressible flow we know:

$$\rho_a \partial(r v_z)/\partial z + \rho_a \partial(r v_r)/\partial r = 0 \qquad (2)$$

where v_r is the radial velocity and ρ_a is the ambient density. Thus in the absence of axial gradients in v_z outside the jet (i.e., where $\partial v_z/\partial z = 0$), the "differential mass flux" $2\pi\rho_a r v_r$ is constant (and negative) outside the jet (this is a reiteration that outside the jet, entrainment remains constant). Any deviation from this value (toward the positive) indicates a positive axial v_z gradient and thus marks the jet boundary according to the jet boundary definition implied by **Eqn. 1**. In the case of self-similarity, theory confirms that $r v_r$ reaches a minimum at the jet boundary. From the jet boundary, moving downstream axially along a constant radial position, the axial velocity must first increase to a peak and then decrease 'self-similarly' (Abramovich, 1963). Accordingly, just inside the jet boundary, $\partial v_z/\partial z > 0$, so continuity demands that $\partial(r v_r)/\partial r < 0$. Hence, moving outward radially toward the jet boundary, $r v_r$ must continue to decrease while $\partial v_z/\partial z > 0$, until we reach the jet boundary where $\partial v_z/\partial z = \partial(r v_r)/\partial r = 0$ and $r v_r$ reaches its minimum.

Under conditions where the axial velocity outside the jet varies, such as for confined flow with chamber-scale recirculation, a similar criterion can still define the edge of the jet. In the ambient gas, viscous effects are minimal, and the recirculating flow in the ambient is driven primarily by pressure gradients. For a chamber of finite radius, $r v_r$ in the ambient flow is necessarily zero at the chamber wall. Moving from the wall toward the jet, chamber-scale recirculation causes negative axial gradients of axial velocity ($\partial v_z/\partial z < 0$, *e.g.*, see axial components of vectors in **Fig. 3**), so continuity demands that $\partial(r v_r)/\partial r > 0$, such that $r v_r$ decreases with decreasing radius. Inside the jet boundary, turbulence/viscous forces entrain flow into the axial direction, causing a large positive axial velocity gradient ($\partial v_z/\partial z > 0$) and turning $r v_r$ back toward zero. That is, when $\partial v_z/\partial z > 0$, continuity demands that that $\partial(r v_r)/\partial r < 0$, such that $r v_r$ reaches a radial minimum moving along the radial coordinate from the wall toward the jet boundary. Hence, similar to the case of an ambient gas with zero axial velocity gradients, the edge of the jet can still be defined as the position where $r v_r$ achieves its minimum value and then starts to increase as the jet boundary is approached radially from outside the jet.

The above definition of the jet boundary is useful for several reasons. First, it does not assume any strict conical shape (or any other shape) for the jet. The jet boundary may have any arbitrary contour as enforced by the physical geometry constraints and fluid mechanics. Second, it applies equally well for confined and unconfined jets, as well as for jets with co-flow. Third, it should be applicable for jet transients, such as the transient deceleration at the end of injection, which is the focus of the current study. Fourth, rather than computing the gradients in velocity, which have relatively high uncertainty, we can rely directly on the velocity map scaled by the local radius. Lastly, any change in the jet boundary caused by deceleration of the flow issuing from the nozzle should be reflected in shifts in the local $r v_r$ radial minima.

An alternative definition of the jet boundary that merits discussion is the radial location where the axial velocity is zero. For confined jets such as in the current study, which generally have a negative axial velocity at the $r v_r$ minima, the position of zero axial velocity is at a smaller radius from the jet axis than the $r v_r$ minimum. The position of zero axial velocity also represents the most upstream position along an entrainment streamline before the jet carries the entrained fluid farther downstream. Hence, the zero-axial-velocity definition of the jet boundary is effectively a relocation of the entrainment flow to the most upstream position along the entrainment streamlines. That is, for different choices of the jet boundary, the distribution of the local entrainment rate along the jet axis altered. Although the integrated entrainment across the *entire* boundary must be identical for any boundary definition (as long as the boundary is not so far inside the jet that the entrained flow never crosses it), recall that we desire the local boundary definition to relate meaningfully to the physical surface through which the entrainment is actually occurring. Therefore some comparison of these definitions with other well known jet visualization data (e.g. schleiren) is desirable.

For either definition of the jet boundary, the differential entrainment rate into a frustum-shaped control volume extending to the jet boundary can be defined as (Han & Mungal, 2001):

$$\frac{d\dot{m}}{dz} = \frac{2\pi\rho_a r v_n}{\cos(\theta)} \qquad (3)$$

where ρ_a is the density in the unmixed ambient, θ is the frustum half-angle, and $v_n = -cos(\theta) v_r + sin(\theta) v_z$ is the normal velocity into the angled frustum surface.

The normalized differential entrainment rate, or "entrainment coefficient" (Han & Mungal, 2001; Ricou & Spalding, 1960) can be defined as

$$C_e = \frac{d\dot{m}}{dz}\frac{d^*}{\dot{m}_0} \quad (4)$$

where $\dot{m}_0$ is the mass flux at the orifice during the relatively steady portion of the injection, and $d^* = d_0\sqrt{\rho_f/\rho_a}$ is the jet orifice diameter d_0 adjusted according to the square root of the ratio of the injected fluid (fuel) density ρ_f to the ambient fluid density ρ_a.

Equation 4 can be applied anywhere in the field, but as described above, it is only a spatially accurate measure of entrainment at the jet boundary. Even so, to better understand the radial and axial flows in the ambient gases that contribute to entrainment, we propose a field visualization of the local mass fluxes. We define a normalized differential mass flux field F_e, expressed as two components $F_{e,r}$ and $F_{e,z}$:

$$F_{e,r} = 2\pi\rho_a r\frac{d^*}{\dot{m}_0}v_r \quad (5)$$

$$F_{e,z} = 2\pi\rho_a r\frac{d^*}{\dot{m}_0}v_z \quad (6)$$

The entrainment at the local jet boundary r_b can be computed from the flux field components $F_{e,r}$ and $F_{e,z}$, consistent with **Eqns. 3** and **4**:

$$C_e(r_b, z) = -F_{e,r}(r_b, z) + tan(\theta)F_{e,z}(r_b, z) \quad (7)$$

Entrainment field visualizations

This work contributes a new, yet straightforward approach for visualizing the jet boundary and computing the axial entrainment distribution along the jet using the full-field entrainment data to determine the jet boundary in a way that is robust to axial gradients.

An example PIV-measured velocity field in a plane passing through the nominal jet axis is presented in **Fig. 4**. The velocity data are ensemble averaged over 40 separate injection events, all acquired at the same 1700μs delay from the commanded start of injection. At this instant in the transient jet development, the head of the jet is still within the measurement plane. As described earlier, although the PIV technique is able to resolve both high velocities within the jet and low velocities outside the jet by using either short- or long-pulse-separation image-pairs, for clarity of presentation, only the low-velocity vectors are included here. In this and in following figures, the high-velocity region where the long-pulse-separation measurements are not reliable is masked off by a white triangle that approximately encompasses the jet interior. The colored contours underlying the velocity vectors represent the radial velocity component, as indicated by the colormap to the right of the image.

To visualize entrainment throughout the ambient domain outside the jet, we apply a transformation to the velocity field to yield the components of F_e. The transformation is accomplished by scalar multiplication of each velocity component, at every measurement point, by the value $\left[2\pi\rho_a r\,\frac{d^*}{\dot{m}_0}\right]$. The result is a vector field of the normalized differential mass flux components, $[F_{e,\mathrm{r}}\hat{\boldsymbol{r}}, F_{e,z}\hat{\boldsymbol{z}}]$. (Notice from **Eqn. 7** that the value of C_e is the dot product of the flux field at the jet boundary with the velocity vector normal to the surface of the frustum.)

Figure 5 presents a contour plot of the result for the radial component, $F_{e,r}$. In the axisymmetric coordinate system, negative values of $F_{e,r}$ in the ambient indicate radial flux directed toward the jet. The contours in **Fig. 5** are similar to those in **Fig. 4**, but the scaling by the radius shifts them outward somewhat, and reduces the radial gradients outside the jet. Also, the contours in **Fig. 5** display some asymmetry, with slightly larger $F_{e,r}$ magnitudes on the right side of the jet. Note, however, that the raw velocity contours in **Fig. 4** display much less asymmetry, especially near the jet. Hence, this increased asymmetry in **Fig. 5** is likely because of misalignment between the coordinate system centerline and the actual jet centerline, so that the matrix multiplication of **Fig. 4** with **Fig. 5** perhaps uses values for the radius from the jet centerline that are too large on the right side and too small on the left. Quantification of this and other sources of uncertainty will be addressed following the results section.

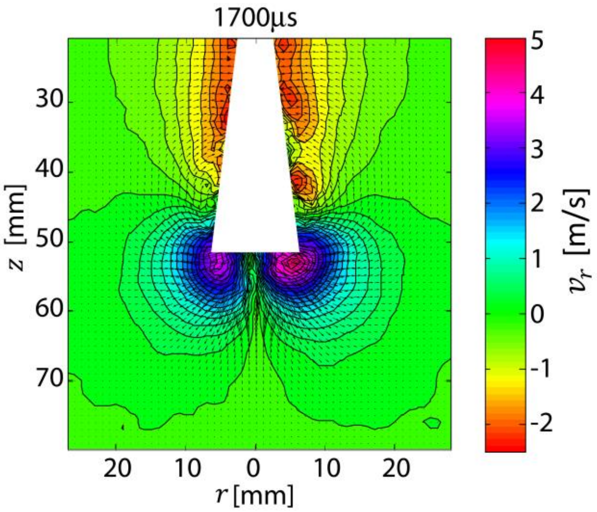

Figure 4. PIV-measured velocity field 1700μs after the commanded start of injection. Each vector in the map is $[v_r\hat{\boldsymbol{r}}, v_z\hat{\boldsymbol{z}}]$, and the contours show the magnitude of the radial velocity component (v_r).

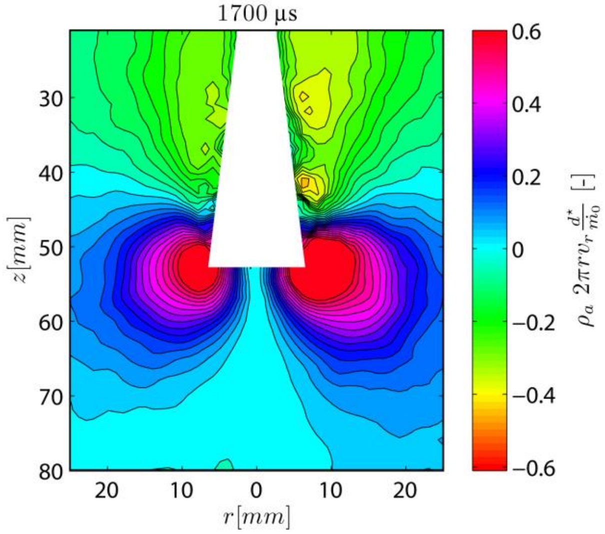

Figure 5. Example field of the radial component of the normalized differential mass flux ($F_{e,r}$). Contours are plotted every 0.04 units.

Quantification of the jet boundary

In the appendix section we describe the qualitative evolution of the flux field during the injection and after the end of injection, but quantifying the evolution of entrainment along the jet requires the position of the jet boundary where C_e can be computed from $F_{e,r}$ and $F_{e,z}$.

As described in the Entrainment quantification section, rv_r (or $F_{e,r}$) reaches a local radial minimum in regions where the axial gradient of v_z (or $F_{e,z}$) is zero, which defines the jet boundary. In **Fig. 6** we show the results of computing $F_{e,r}$ at the axial position z = 20mm for different instants spanning from the start of injection to the final transient after the end of injection (gray lines). Selected profiles of $F_{e,r}$ corresponding to measurement timings during the quasi-steady period of transient jet (black lines, see Appendix B for definition of quasi-steady conditions) are averaged to yield the time-averaged profile of $F_{e,r}$(red line). The radial minimum (blue circle) of the $F_{e,r}$ time-average corresponds to the location where C_e is computed from the F_e components according to **Eqn. 7**.

A computation of those average local minima at different axial distances yields a profile of the *quasi-steady* jet boundary, shown as black dots in **Fig. 7**, as well as *instantaneous* jet boundaries when considering the minima of individual profiles of $F_{e,r}$ (not shown).

Although more complex shapes are possible, in this case, we have assumed a cone-shaped jet boundary anchored at the injector (red dashed lines in **Fig. 7**) to compute a single average jet-boundary spreading half-angle, α (see **Fig. 3**). With such a computation, the angle is 10.2°. This value is very close to the value of 10.25° measured for this injector, in the same conditions, using schlieren imaging (Malbec *et.al.*, 2013). Using the alternative jet boundary, where the axial velocity is 0 gives an α of 10.9°. This is slightly higher but still very close to the value obtained with schlieren images. Based on the discussion in the *Entrainment quantification* section, a larger jet angle is expected when computed with the minimum $F_{e,r}$. This is indeed the case in the far field (*e.g.* z > 50mm in Figure 8), but the method used to computed the jet angle seems to minimize this effect.

It is interesting that 3 different diagnostics provide values for α that are so close. However, in both in the PIV and schlieren techniques, the jet angle is defined under the assumption that the best fit for the jet boundary is a cone whose origin is coincident with the nozzle tip, therefore strong variation would have been more unusual. More significant is that a single cone angle presumes that the jet boundaries *should* be straight. Perhaps an alternate, continuum surface would produce better correlation between the local entrainment and a local jet spreading-angle. The implications of this observation are not explored here.

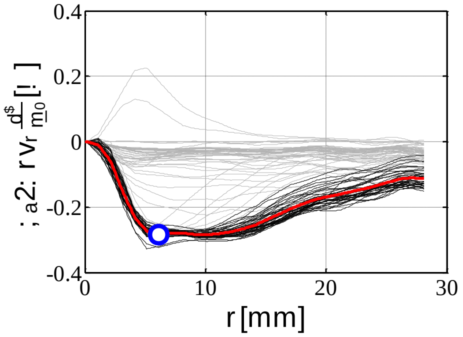

Figure 6. Instantaneous and averaged $F_{e,r}$ showing the radial location of the quasi-steady jet boundary at an axial distance of 20mm. Grey lines present the evolution of the profile during different instants throughout the whole measurement period. Black lines correspond to the profiles during the quasi-steady (as defined in Appendix B), and the red line is the average of the black lines. The blue circle defines the position of the local minimum of the red line, indicating the jet boundary where we compute C_e.

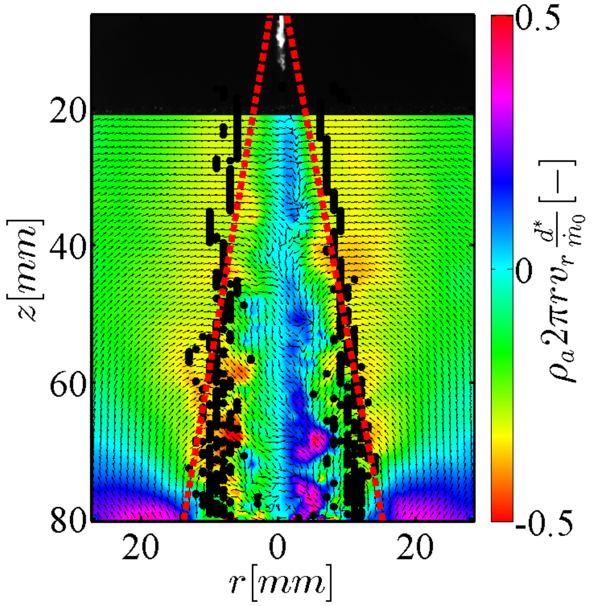

Figure 7. Black dots: Positions of the quasi-steady jet boundary. Dashed red lines: approximation of the quasi-steady boundary by a cone-shaped control surface with its vertex anchored at the injector orifice.

Both definitions thus seem to provide reasonable jet boundary estimations. However, continuity of the jet boundary is also desirable to avoid missing integral contributions to the entrainment rate. Therefore, the cone-shaped control surfaces will be used to compute the air entrainment in the next section. Note, however, that the conical boundary with the vertex anchored at the injector orifice does not match the angle of the line of quasi-steady $F_{e,r}$ minima (black dots in **Fig. 7**) very well. It appears that a smaller cone angle, with a vertex farther upstream of the orifice, would produce a better fit. Further implications of this observation are not explored here. Also, closer to the injector, string of quasi-steady $F_{e,r}$ minima are essentially parallel to the radius, and finding a unique location where the axial velocity is zero for the alternative jet-boundary definition is also difficult.

After the end of injection, the two jet boundary definitions yield much different evolutions of the instantaneous jet boundaries during and after passage of the entrainment wave. **Figure 8** shows that before the end of injection, the boundaries are similar for the two definitions. After the end of injection, upstream of the entrainment wave, the jet width increases, and it is much wider using the jet boundary based on zero axial velocity. In this respect only the minimum rv_r definition is representative of behavior seen in schlieren images after the end of injection.

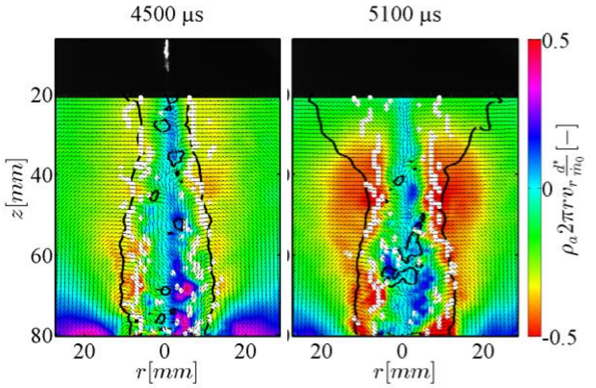

Figure 8. Comparison of instantaneous jet boundaries before (left) and after (right) the end of injection, computed with the 2 proposed definitions. Black line: axial velocity definition; white dots: minimum rv_r definition. Note 5100μs is after the end of injection.

Results: Entrainment profile comparisons

With the jet boundaries and corresponding control surfaces defined, the variation of the entrainment coefficient along the jet axis $C_e(z)$ can be computed as defined in **Eqn. 7**. For this computation, the conical control-surface fit (red line in **Fig. 7**) to the individual $F_{e,r}$ values that define the jet boundary. The results are presented in **Fig. 9**, which shows the axial evolution of $C_e(z)$ at different instants before the end of injection. The negative values are due to the head of the spray, which has strong flow radially outward. After the passage of the head of the jet, $C_e(z)$ is virtually constant, both along the jet axis and in time as long as the injection is sustained. The transient region typically observed near the nozzle, where $C_e(z)$ has a lower value (Han & Mungal, 2001; Hill, 1973), does not appear in **Fig. 9**, probably because the measurements are downstream this region (in our case, $z > 40d^*$).

A comparison between the value of $C_e(z)$ given by the 1-D spray model and the quasi-steady portion of the injection is provided in **Fig. 9**. The model uses the experimental conditions and measured injection rate as inputs, and uses an assumed jet boundary half-angle of α=10.5°. The experimental and modeled values are remarkably similar. The mean of the experimental $C_e(z)$ in the quasi-steady portion of the jet is approximately 0.28 for both the model and the experiment, which is slightly lower than the typical 0.32 value for gas jets (Han & Mungal, 2001; Ricou & Spalding, 1960). However, for diesel sprays, $C_e(z)$ is, to some degree, a characteristic of the internal flow through the nozzle orifice. Different nozzles, which are known to yield different spray angles, and thus different air entrainment, must have different values of C_e.

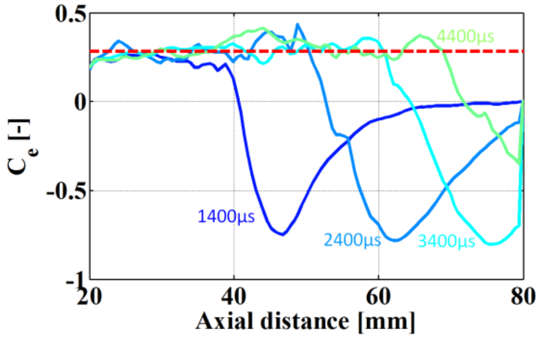

Figure 9. $C_e(z)$ at different times during injection (solid lines). Comparison with the quasi-steady behavior computed with the 1D spray model (red dashed line).

As described earlier, the 1D spray model predicts an entrainment wave of temporarily increased entrainment that travels downstream through the jet after the end of injection. Until now, no experimental evidence has been produced to validate this prediction in diesel jets. Details of this entrainment wave is explored in qualitative detail in the appendix discussion of the full-field $F_{e,r}$ and $F_{e,z}$ visualizations. In **Fig. 10** we show a quantitative comparison between experimental and modeled evolutions of $C_e(z)$, or F_e along the jet boundary, after the end of injection.

The evolution of the measured entrainment clearly shows an increase of C_e compared to the quasi-steady value, by a factor of approximately two. Additionally, the magnitude of the maximum entrainment increases as it moves downstream in both the model and the experiments. In the experiments, the region with temporarily increased entrainment has a wide axial extent, spanning over 40mm at 5000µs and 5500µs after the commanded start of injection. For the model, the magnitude of the entrainment wave peak is 2.5 times that of the quasi-steady-steady jet, slightly higher than in the experiments, and its axial extent is also smaller. Fluid mechanical processes occurring in the real jet that are absent from the 1D model may distribute the entrainment wave over a greater axial extent, thereby also lowering its peak value. Similar conclusions were offered in a Reynolds averaged Navier-Stokes (RANS) simulation of a different transient jet (Singh & Musculus, 2010). Though the peak magnitudes and spatial extents of the measured and predicted entrainment waves are different, the time-integrated entrainment during the transient increase above the steady jet (not shown) is nearly identical for model and experiment. Another difference is the fact that the peak in the modeled entrainment wave moves downstream faster than the experimental one. The confinement of the jet by the chamber, which is not included in the 1D model, likely contributes to some of this difference, but a further analysis of the data is required to be conclusive.

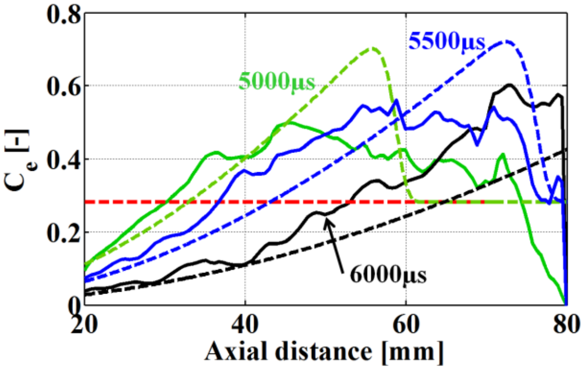

Figure 10. Measured (solid lines) and modeled (dashed lines) axial evolution of $C_e(z)$ for different timings *after* the end of injection.

Limitations and uncertainty

One drawback of the PIV technique can be the inability to measure velocities close to zero. Here, the absolute uncertainty in the PIV has been quantitatively determined based on the random fluctuations measured in the near-zero velocity field before the beginning of injection. The measured root mean squared velocity is 0.07m/s when it should have recorded zero. Expanding C_e at the normalization condition at the jet boundary, we obtain a simplified form for the equation:

$$C_e = \frac{r v_r}{U_o}\left(\frac{\rho_a}{\rho_f}\right)^{1/2}$$

In **Table 1**, estimates of the precision and the computed sensitivities of the entrainment coefficient are tabulated. From these contributions to error in C_e, we see that deviation in the jet properties from their reference values are more dominant sources of uncertainty than the velocity field.

Parameter	**Precision**	**Error Sensitivity**	**Relative uncertainty**
Ambient density	0.3kg/m^3	0.5	0.7%
Fuel density	15kg/m^3	0.5	1.1%
Velocity	0.07m/s	1	3%
Jet position	1e^{-4} m	1	10%
Initial jet Velocity	30m/s	1	6%
Total Uncertainty			12.1%

As with previous quantifications of entrainment, this method is subject to uncertainty in the jet position and angle relative to the PIV data plane. As described earlier, one manifestation of a misalignment is apparent jet asymmetry. Also, in the far-field of a steady jet, the entrainment predicted by the 1D model should be a constant. Deviation from a constant value could be due to real fluid-mechanical effects, like three-dimensional flows (velocities in the theta direction of the cylindrical coordinate system, which are not measured as assumed zero) or the effects of confinement by the finite chamber volume, or diagnostic issues with poorly resolved low velocities outside the jet.

For our PIV measurements, particles of zirconium oxide of diameter $d_p = 5\mu m$ and density $\rho_p = 5680\ kg/m^3$ are seeded into the ambient gases. To determine how well these particles match the flow velocities, the Stokes time constant τ_p is computed for these particles, $\tau_p = \rho_p d_p / 18\mu_a$. At an ambient-gas temperature of 900K, we assumed an ambient viscosity of $\mu_a = 3.63 \times 10^{-5}$ Pa-s, which yields $\tau_p = 2.17 \times 10^{-4}$s. During flow development, inversion of the average quasi-steady-ensemble velocity gradients outside the spray provides an estimate of the average flow acceleration at the jet boundary. Expressed as a flow timescale $\tau_f = \Delta r / \Delta v_z = \frac{0.005m}{1m/s} = 5 \times 10^{-3} s$. This gives a Stokes number near the jet boundary of $St = \tau_p / \tau_f = 0.043$. For *St* < 0.5, particles have been shown to reliably follow the flow, although a better target may be *St* < 0.01 (Clemens and Mungal, 1991). Inside the jet boundary, however, and including at the region where v_z=0 was determined, much larger gradients are experienced, and the reliability of the PIV decreases due to an increased velocity lag of the particles.

Near the injector orifice, we know that the gradients increase very rapidly (over spatial scales < 1mm). Certainly when the interface is smaller than the PIV resolution, a biased velocity lag will result. However, as the jet develops downstream, the growing interface region smears these gradients, and in the regions of the flow presented, we believe the presented data at the jet boundary reliable. A more detailed analysis is planned for a future publication on how the particle lag contributes to error in entrainment rate under the decelerating jet (accelerating entrainment) conditions of the entrainment wave.

Summary and conclusions

Prior work that proposed to calculate jet entrainment by measuring either the axial momentum gain within the jet or ambient flows toward the jet presumed that outside the jet there are no axial variations in the ambient. Although this assumption does not affect measurements of total entrainment over the whole jet, only by determining an accurate estimate for the local jet boundary, r_b, can the local entrainment be properly determined. In the previous cases of free-jets, this jet boundary can be functionally determined as the position where rv_r first reaches its minimum. Even for the case of confined jets, in the presence of significant axial and radial gradients measured in the present experiment, the minimum rv_r compares favorably to previous estimates of the jet boundary made from Schlieren visualizations.

Using this new definition for the spray boundary, we compared the measured local entrainment of a transient injection to the predictions of a simplified 1D jet model to confirm the existence of an entrainment wave after the end of injection. We found quantitative agreement in the quasi-steady jet entrainment and qualitative agreement in the transient entrainment increase due to the entrainment wave after the end of injection. The peak local entrainment increase above that of a quasi-steady jet in the experiment is only about 2/3 of that predicted by the 1D model, and the duration of the local entrainment increase is longer in the experiment. Nevertheless, the measured time-integrated entrainment increase after the end of injection matches the predictions well, indicating that only the distribution of the entrainment wave and not its total effect are different than predicted. Fluid mechanical processes occurring in the real jet, which are not included in the 1D model, may be responsible for the wider distribution of entrainment than predicted by the model. We speculate that the effect of confinement on this jet may also play a role, but more work is needed to clarify the respective effects.

Acknowledgements

All of the PIV experimental work was performed at IFP Énergies nouvelles. Much of the analysis of the IFPEN PIV dataset was performed at the Combustion Research Facility, Sandia National Laboratories, Livermore, CA. Support was provided by the U.S. Department of Energy, Office of Vehicle Technologies. Sandia is a multi-program laboratory operated by Sandia Corporation, a Lockheed Martin Company for the United States Department of Energy's National Nuclear Security Administration under contract DE-AC04-94AL85000.

Nomenclature

C_e	jet entrainment Coefficient
d	diameter
F_e	differential mass flux field
m	mass
r	radius from jet centerline
Re	Reynolds number
St	Stokes number
ρ	density
μ	viscosity
v	jet velocity
τ	timescale

Subscripts

a	ambient (chamber gasses)
f	fuel (diesel)
p	particle
r	radial derivative
z	axial derivative
b	jet boundary

Acronyms

ECN	Engine Combustion Network
IFPEN	IFP Energies Nouvelles
LDV	Laser Doppler Velocimetry
PIV	Particle Image Velocimetry

References

Abramovich, G. N. (1963). *The theory of turbulent jets*. Cambridge, Massechusetts: The M.I.T. Press, p. 10-14.

Bisset, D. K., Hunt, J. C. R., & Rogers, M. M. (2002). The turbulent/non-turbulent interface bounding a far wake. *Journal of Fluid Mechanics*, *451*, 383–410. doi:10.1017/10.1017/S0022112001006759

Boree, J., Atassi, N., & Charnay, G. (1996). Phase averaged velocity field in to a sudden velocity decrease. *Experiments in Fluids, 21*, 447–456.

Curtet, R., & Ricou, F. P. (1964). On the tendency to self-preservation in axisymmetric ducted jets. *Journal of Fluids Engineering*, *86*(4), 765–771. doi:10.1115/1.3655947

Clemens, N. T., & Mungal, M. G. (1991). A planar Mie scattering technique for visualizing supersonic mixing flows, *Experiments in Fluids 11,* 175–185.

Dahm, W. J. A., & Dimotakis, P. E. (1987). Measurements of Entrainment and Mixing in Turbulent Jets. *AIAA Journal*, *25*(9), 1216–1223.

Desantes, J. M., Arrègle, J., López, J. J., & Cronhjort, A. (2006). Scaling laws for free turbulent jets and diesel-like sprays. *Atomization and Sprays*, *16*, 443–474.

Engine Combustion Network. (n.d.). Retrieved from http://www.sandia.gov/ecn/

Han, D., & Mungal, M. G. (2001). Direct measurement of entrainment in reacting/nonreacting turbulent jets. *Combustion and Flame*, *124*, 370–386. doi:10.1016/S0010-2180(00)00211-X

Hu, B., Musculus, M. P. B., & Oefelein, J. C. (2010). Large eddy simulation of a transient air jet with emphasis on entrainment during deceleration. *SAE Technical Paper*, *2010-01-11*.

Hill, B. J. (1973). Measurement of local entrainment rate in the initial region of axisymmetric turbulent air jets. *Journal of Fluid Mechanics*, *51*(4), 773–779.

Iyer, V., & Abraham, J. (2005). Two-fluid modeling of spray penetraiton and dispersion under diesel engine conditions. *Atomization and Sprays*, *15*, 249–270.

Kozma, J. H., & Farrell, P. V. (1997). Air entrainment in a high pressure diesel spray. *SAE Technical Paper*, *971620*. doi:10.4271/971620

Malbec, L., & Bruneaux, G. (2010). Study of air entrainment of multi-hole diesel injection by particle image velocimetry - effect of neighboring jets interaction and transient behavior after end of injection . *SAE Int. J. Engines*, *3*(1), 107–123.

Malbec, L.-M., Egúsquiza, J., Bruneaux, G., & Meijer, M. (2013). Characterization of a set of ECN spray A injectors: nozzle to nozzle variations and effect on spray characteristics. *SAE Int. J. Engines*, *6*(3), 1642–1660. doi:10.4271/2013-24-0037

Milano, P., Brunello, G., & Coghe, A. (1991). LDV Characterization of Air Entrainment in Transient Diesel Sprays. *SAE Technical Paper*, *910178*.

Moon, S., Matsumoto, Y., & Nishida, K. (2009). Entrainment, Evaporation and Mixing Characteristics of Diesel Sprays around End-of-Injection. *SAE Technical Paper*, *2009-01-08*. doi:10.4271/2009-01-0849

Musculus, M. P. B. (2009a). Entrainment waves in decelerating transient turbulent jets. *Journal of Fluid Mechanics*, *638*, 117. doi:10.1017/S0022112009990826

Musculus, M. P. B., & Kattke, K. (2009a). Entrainment Waves in Diesel Jets. *SAE Int. J. Engines*, *2*(1), 1170–1193. doi:10.4271/2009-01-0849

Musculus, M. P. B., Miles, P. C., & Pickett, L. M. (2013). Conceptual models for partially premixed low-temperature diesel combustion. *Progress in Energy and Combustion Science* (Vol. 39, pp. 246–283). Elsevier Ltd. doi:10.1016/j.pecs.2012.09.001

Nickels, T. B., & Perry, a. E. (1996). An experimental and theoretical study of the turbulent coflowing jet. *Journal of Fluid Mechanics*, *309*, 157–182. doi:10.1017/S0022112096001590

O'Connor, J., & Musculus, M. (2013). Post Injections for Soot Reduction in Diesel Engines: A Review of Current Understanding. *SAE Int. J. Engines*, *6*(1), 400–412. doi:10.4271/2013-01-0917

Philip, J., & Marusic, I. (2012). Large-scale eddies and their role in entrainment in turbulent jets and wakes. *Physics of Fluids*, *24*(5), 055108. doi:10.1063/1.4719156

Post, S., Iyer, V., & Abraham, J. (2000). A Study of Near-Field Entrainment in Gas Jets and Sprays Under Diesel Conditon. *Journal of Fluids Engineering*, *122*, 385–395.

Rhim, D., & Farrell, P. V. (2000). Characteristics of Air Flow Surrounding Non- Evaporating Transient Diesel Sprays. *SAE Technical Paper*, *2000-01-27*. doi:10.4271/2000-01-2789

Ricou, F. P., & Spalding, D. B. (1960). Measurements of entrainment. *Journal of Fluid Mechanics*, *11*(1), 21–32.

Siebers, D. L. (1999). Scaling Liquid-Phase Fuel Penetration in Diesel Sprays Based on Mixing-Limited Vaporization. *SAE Technical Paper 1999-01-0528*. Doi:10.4271/1999-01-0528

Singh, G., Sundararajan, T., & Bhaskaran, K. a. (2003). Mixing and Entrainment Characteristics of Circular and Noncircular Confined Jets. *Journal of Fluids Engineering*, *125*(5), 835. doi:10.1115/1.1595676

Singh, S., & Musculus, M. P. B. (2010). Numerical Modeling and Analysis of Entrainment in Turbulent Jets After the End of Injection. *Journal of Fluids Engineering*, *132*(8), 081203. doi:10.1115/1.4002184

Van Dyke, M. (1982). *An Album of Fluid Motion* (p. 99). Stanford, CA: The Parabolic Press.

Appendix A: Entrainment Field Visualization

The spatial and temporal development of $F_{e,r}$ and $F_{e,z}$ during injection appear in **Figs. 12** and **13**, and after the end of injection in **Figs. 14** and **15**. Although data were collected every 100 µs, the data are presented here at wider intervals. We present every 400µs during injection (recall start of injection at 350µs) and every 200µs shortly after the end of injection(at 4600µs), with an increase to 400µs after 5600µs. From **Fig. 12**, we conclude that during the flow development, $F_{e,r}$ is relatively constant over a small region near the jet boundary and upstream of the head vortex. For example, in the 2400 microsecond image of **Fig. 12**, $F_{e,r}$ is relatively uniform from roughly z = 20 to 50mm downstream and at radii from the jet boundary to about r = 10-15mm from the jet centerline. As described in the Entrainment quantification section, when the axial velocity is axially invariant in the ambient, rv_r, and hence $F_{e,r}$, is constant radially. At those axial locations at large radii however, the $F_{e,r}$ departs from its local minimum (*i.e.* $\partial(rv_r)/\partial r > 0$) which by continuity implies that in this region $\partial(v_z)/\partial z < 0$. Indeed, an axial gradient in $F_{e,z}$ is apparent in **Fig. 13**, likely caused by chamber-scale recirculation.

As described in the Entrainment quantification section, the minimum in rv_r, or equivalently in $F_{e,r}$, is one definition of the jet boundary, and recall that only at the jet boundary is the correct entrainment rate measured. In the last image of Fig. 12, the minimum generally occurs at the interior edge of the yellowish or light-green contour, for which $F_{e,r}$ is roughly -0.3, corresponding to $C_e = 0.3$. Additionally, rv_r (or $F_{e,r}$) reaches a local radial minimum in regions where the axial gradient of $F_{e,z}$ is non-zero in **Fig. 13**. Furthermore, the radial minimum in $F_{e,r}$ generally is in the same vicinity as the minimum $F_{e,z}$.

The entrainment coefficient C_e includes contributions from both the radial and axial components of F_e. However, at a typical jet-boundary angle near 10°, the contribution of $F_{e,z}$ to C_e is only about 17% (**Eqn. 7**), such that C_e is dominated by $F_{e,r}$. The value of $F_{e,r}$ (and hence, C_e) near 0.3 is typical of momentum-driven, turbulent non-reacting jets (Han & Mungal, 2001; Ricou & Spalding, 1960).

After the end of injection (**Fig. 14)**, the peak magnitude of $F_{e,r}$ increases ($F_{e,r}$ becomes more negative) relative to the preceding quasi-steady level. This entrainment increase propagates downstream with time. ($F_{e,z}$ remains small near the jet-boundary minimum $F_{e,r}$, so that C_e continues to be dominated by $F_{e,r}$.) As described in the introduction, this transient entrainment wave was predicted by previous 1D jet model analyses (Musculus & Kattke, 2009; Musculus, 2009). In addition to the transient increase in entrainment after the end of injection, the apparent jet boundary in the $F_{e,r}$ and $F_{e,z}$ fields in **Figs. 14** and **15**increases, especially in the upstream region. Though the $F_{e,r}$ contours in **Fig. 14** often show multiple minima along some radial paths, the $F_{e,r}$ radial minimum generally moves outward after the entrainment wave passes. In some instances, such as at 7200 or 8000µs, the radial minima at axial positions near 20 mm downstream appear to be outside the field of view. The zero axial velocity definition of the jet boundary also yields an increase in the jet width after the end of injection. This boundary is indicated by the $F_{e,z} = 0$ contour in **Fig. 15**. In particular, the 5000µs image in Figure 14 shows a clear increase in the jet boundary radius at the $F_{e,z} = 0$ contour to approximately 10mm in the upstream region, and by 8000µs the contour has progressed to a 20mm radius in the near field

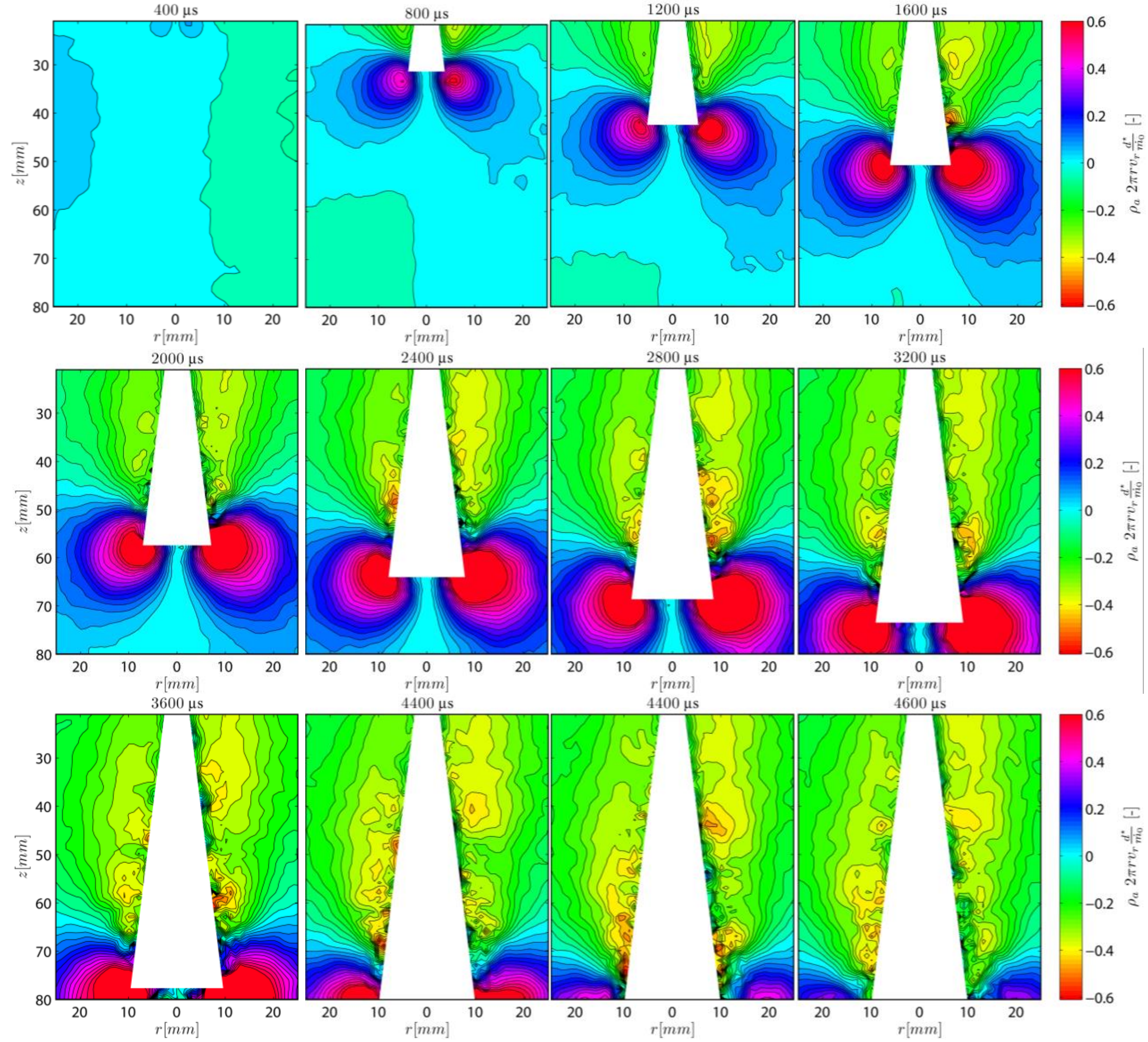

Figure 11. Developing field of the differential radial mass flux ($F_{e,r}$) at various times during injection (350-4600µs after the start of injection). Data from the jet interior are whited out due to lack of correlation in PIV data.

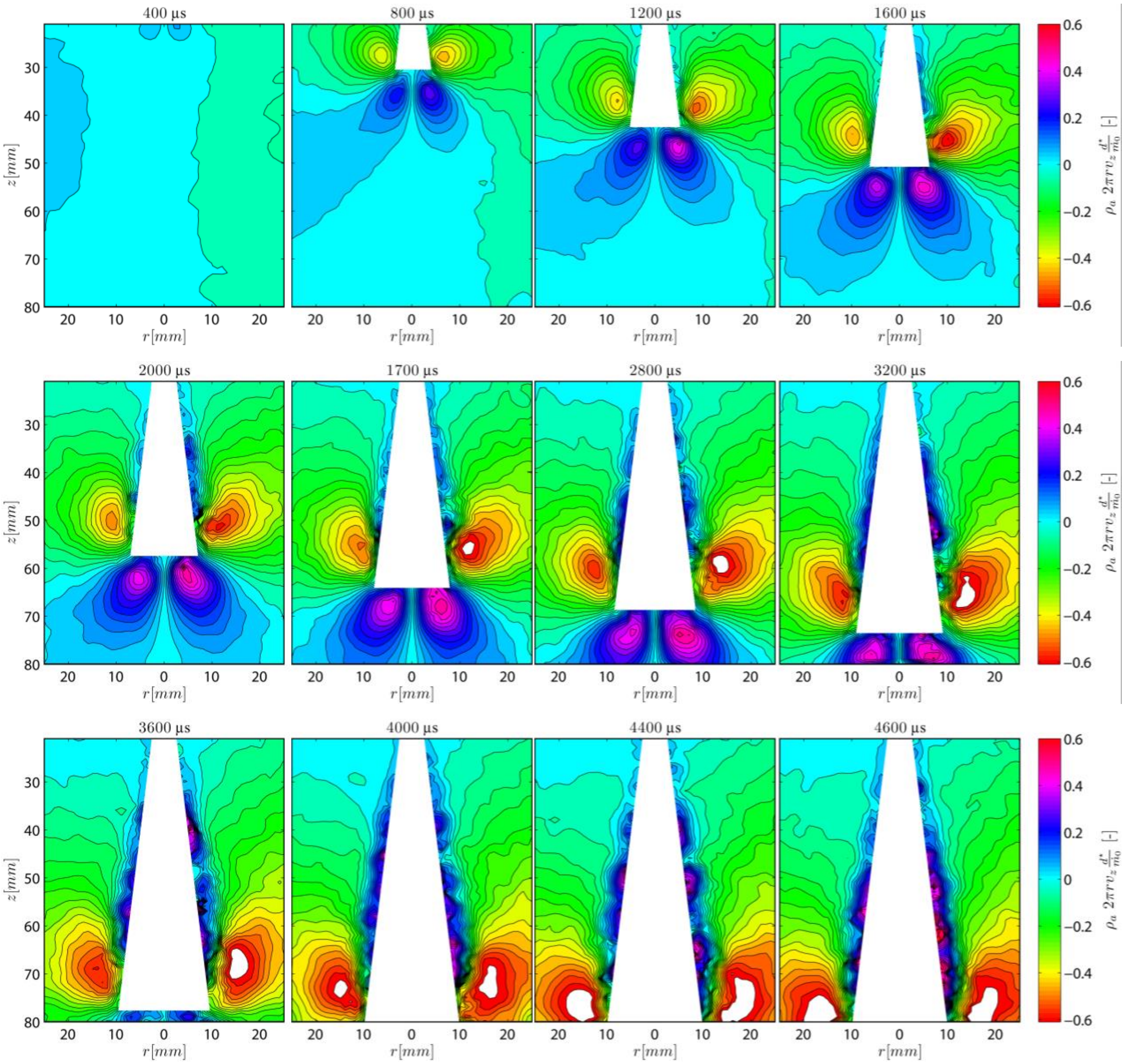

Figure 12. Developing field of the differential axial mass flux ($F_{e,z}$) at various times during injection (350-4600 μs).

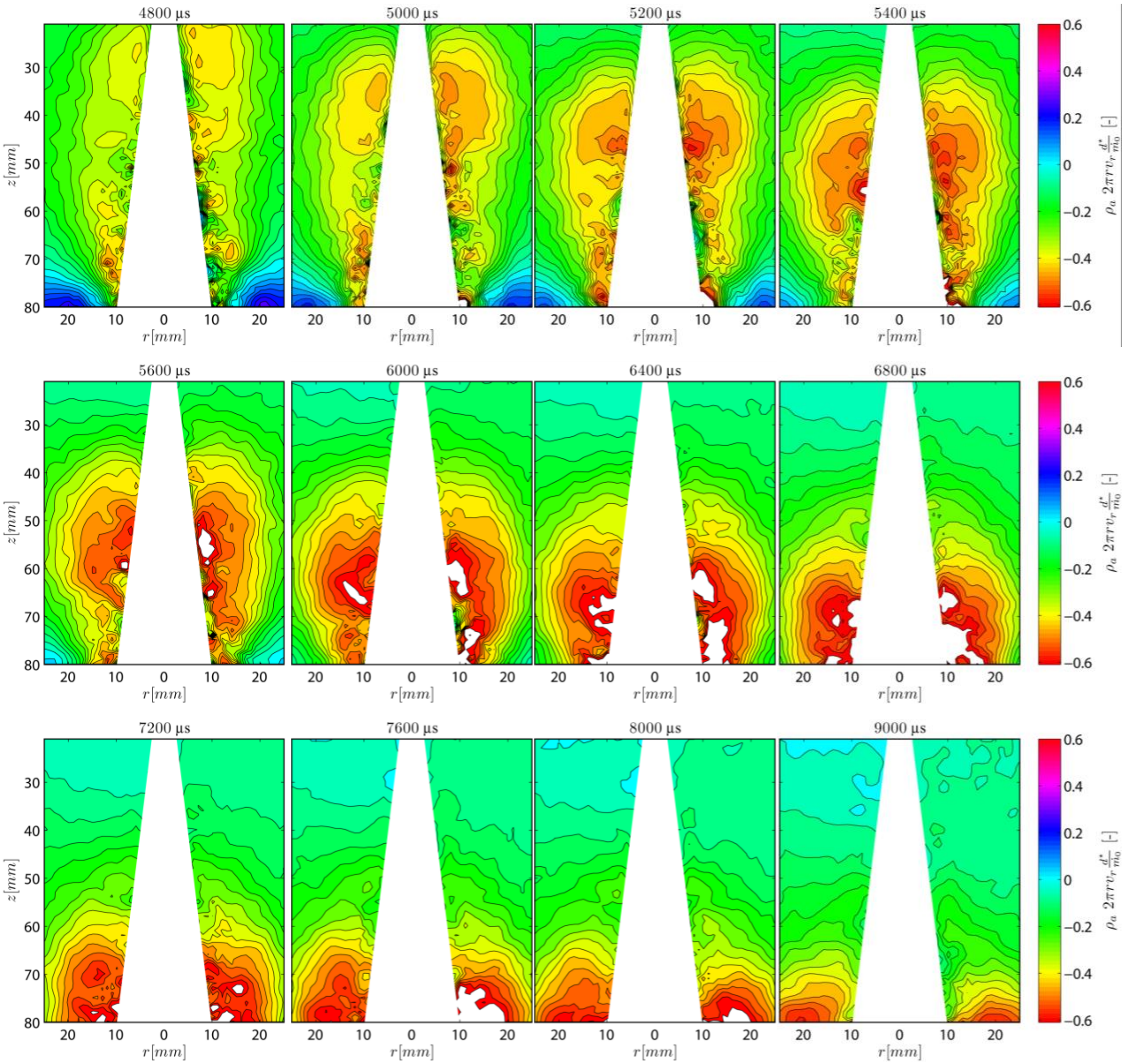

Figure 13. Developing field of the differential radial mass flux ($F_{e,r}$) after the end of injection (4800-9000 µs after the start of injection).

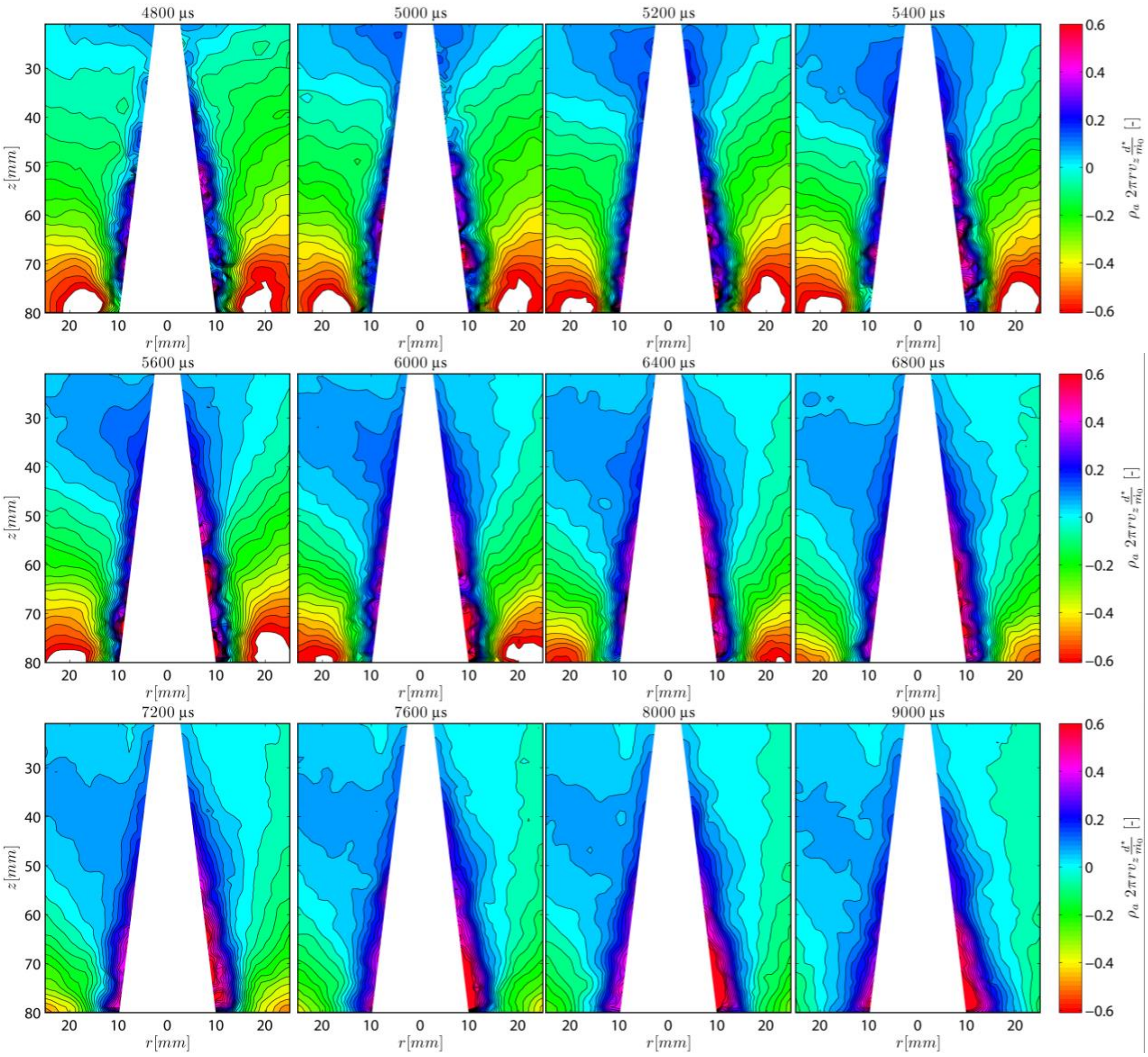

Figure 14. Developing field of the differential axial mass flux ($F_{e,z}$) after the end of injection (4800-9000 µs after the start of injection).

Appendix B: Definition of the quasi-steady behavior of the jet

In this appendix we describe how we determined the time interval over which the differential radial mass flux field, $F_{e,r}$, and hence the jet boundary is considered quasi-steady. The difficulty lies in defining when during the injection the local values reach and then depart from a quasi-steady. Between these two events is the quasi-steady period. These instants are specific to each axial location, e.g. closest to the nozzle tip, the quasi-steady is reached sooner and departed from sooner.

The criteria that has been defined uses the minima found from $F_{e,r}$. Here we examine the time dependence of the minima $F_{e,r}(t,r,z)$. To demonstrate the method, we focus on a single axial distance (z = 30mm), although the procedure was repeated at each axial location. In **Fig. 16** we plot a normalized histogram of the values attained by $F_{e,r}$ at r =10mm. Before the passing of the head of the jet, $F_{e,r}$ is near zero or positive. During the quasi-steady (see Appendix A), the $F_{e,r}$ has a broad plateau just outside the jet boundary, near the value of 0.3. All profiles for which the value of $F_{e,r}(r,z)$ lies within 10% of this value are averaged. In **Fig. 7** in the text, these profiles are plotted in solid black. The red curve is the ensemble average of all of the black curves during this quasi-steady period. Finally, the open dot at the minimum of the red curve is the computed quasi-steady jet boundary. Notice some values of $F_{e,r}$ indicate larger entrainment (below -0.33). These histogram contributions occur after the end of injection and indicate the transient entrainment wave.

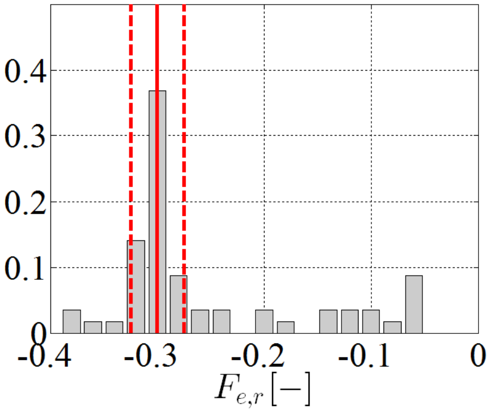

Figure 15. Normalized histogram of $F_{e,r}(t,r=10\text{mm},z=30\text{mm})$ with bin widths of 0.02 $F_{e,r}$. Solid red line is the position of the maximum and dashed red lines are values used to determine the time interval considered the quasi-steady.